HOKKAIDO UNIVERSITY

Title	Mapping the FTS SWIR L2 product of XCO2 and XCH4 data from the GOSAT by the Kriging method : a case study in East Asia
Author(s)	Liu, Yang; Wang, Xiufeng; Guo, Meng; Tani, Hiroshi
Citation	International Journal of Remote Sensing, 33(10), 3004-3025 https://doi.org/10.1080/01431161.2011.624132
Issue Date	2011-10-18
Doc URL	http://hdl.handle.net/2115/50312
Rights	This is an Author's Accepted Manuscript of an article published in International Journal of Remote Sensing Volume 33, Issue 10, pages 3004-3025, 2011, copyright © Taylor & Francis, available online at: http://www.tandfonline.com/10.1080/01431161.2011.624132
Type	article (author version)
File Information	IJRS33-10_3004-3025.pdf

Mapping the FTS SWIR L2 product of XCO_2 and XCH_4 data from the GOSAT by the Kriging method– A case study in East Asia.

Yang LIU * †, Xiufeng WANG ‡, Meng GUO † and Hiroshi TANI ‡

†Graduate school of Agriculture, Hokkaido University, Sapporo, Japan
‡Research Faculty of Agriculture, Hokkaido University, Sapporo, Japan

_____

* Corresponding author. E-mail: yangliu315@hotmail.co.jp

Abstract

Developed by Japan, the Greenhouse Gases Observing Satellite (GOSAT), also known as IBUKI, was successfully launched on January 23, 2009 and is used to monitor greenhouse gases on the Earth's surface. Observations started in April 2009, and the Level 1, Level 2 and Level 3 products became available to general users in November 2009, February 2010 and October 2010, respectively. For this paper, Kriging methods were proposed to generate the spatial distribution of the daily GOSAT's XCO_2 and XCH_4 data within the region of East Asia from June 2009 to May 2010. The relationship between the distance and the difference of the daily data in each month were represented by variogram models. The concentration distributions of XCO_2 and XCH_4 in East Asia can be intuitively seen on a Kriging interpolation map. Seasonal changes were observed. The concentration of XCO_2 was high in winter and spring, which might due to the smoke and dust from coal burning. The concentration of XCH_4 changed significantly with latitude in autumn and winter, mainly according to temperature change. In addition, by comparison, the Level 2 Kriging interpolation values were lower than the ground observed data and consistent with the higher tendency of Level 3 data.

1. Introduction

With the continuous development of human society and associated increase in industrialization, atmospheric concentrations of carbon dioxide (CO_2) and methane (CH_4) have also increased (IPCC FAQ 7.1 2007). According to the World Data Centre for Greenhouse Gases (WDCGG) analysis, the average CH_4 concentration across the world was 1797 parts per billion (ppb) in 2008. This value was an increase of 151% from the average value for the 18th century (715 ppb).

The current concentration of CO_2 is 385.2 parts per million (ppm) which is 2.0 ppm more than it was in 2007. The current concentration has increased 38% from the pre–industrial global level of 280 ppm. In recent years, due to a series of environmental changes caused by this increase, the greenhouse effect has received increased attention (Kondratyev and Varotsos 1995, Varotsos *et al*. 2007). For example, the Kyoto Protocol was signed in Japan in 1997 and focused on the possibility of adopting a requirement to reduce levels by 5% relative to the 1990 level, but there was no noticeable progress with CO_2 emissions reduction (Varotsos 2002). At the opening of the United Nations Climate Change Conference in Copenhagen in 2009, determining how to reduce greenhouse gas (GHG) emissions was included in the agenda of the participating countries, but there, no substantial progress was made.

Asia has the third largest nominal Gross Domestic Product (GDP) of all the continents, after North America and Europe. The largest economies in Asia include China, Japan, India, South Korea and Indonesia, which are all in this study region. The collective economic activity of the region represents roughly 25% of the global domestic product. Rapid growth in large regional economies such as China and India has elevated human prosperity (Preston *et al*. 2006). According to World Bank statistics from 2008, China's and India's populations were 132,564 million and 113,996 million, respectively, which accounted for 36.8% of the total world population. Thus, a study of this region's GHG (greenhouse gas) emissions has great significance for understanding global climate change.

As an important way to address this problem, satellite monitoring plays a crucial role in the observation and assessment of global GHG because nadir satellite remote sensing measurements can observe the GHG molecules in the entire air column (Buchwitz *et al.* 2007). Scanning Imaging Absorption Spectrometer for Atmospheric CHartographY (SCIAMACHY) on Environmental Satellite (ENVISAT), which was an earth–observing satellite instrument launched on March 1st, 2002 (Cracknell and Varotsos 2007), makes necessary observations of CO_2 and O_2 absorptions of the backscattered solar radiation in the near–infrared (NIR) and shortwave infrared (SWIR) (Buchwitz *et al*. 2005). This requires high accuracy and sensitivity to near–surface GHG concentrations. The latest satellite instrument with high surface GHG

sensitivity since the SCIAMACHY on ENVISAT is the Greenhouse Gases Observing Satellite (GOSAT).

The GOSAT was jointly developed by Japan's Ministry of the Environment (MOE), National Institute for Environmental Studies (NIES), and Japan Aerospace Exploration Agency (JAXA) to observe concentrations of CO_2 and CH_4 from space (Yokota *et al.* 2004). It was launched on January 23, 2009, and orbits the earth in roughly 100 minutes at an altitude of approximately 666 km returning to the same orbital path in three days. The observations from the GOSAT are being processed to generate the initial results for CO_2 and CH_4 column–averaged dry–air mole fractions (hereafter referred to as XCO_2 and XCH_4, respectively), which are calculated from the GOSAT radiant spectrum data obtained under cloud–free conditions (Akihiko *et al.* 2009).

The global grid Level 3 data are generated by interpolating and extrapolating the Level 2 data and estimating the distribution of GHG concentrations on a global scale. And also, due to some uncertain factors such as the cloud coverage, observation points are positioned irregularly and the Level 2 data contain extremely high or low values. Therefore, the establishment of a method that generates the distribution map of XCO_2 and XCH_4 data from irregular observation points is being considered. This article combines the GOSAT Level 2 data with the Kriging method to analyse the spatial variations and distributions of GHG throughout the land surface in the regional scale. The Kriging method is a technique that was first developed for the applied fields of mining and geology (Journel and Huijbregts 1978). Since its development, this spatial information science has not only been applied in geology, but has also been widely used in soil science, agriculture, meteorology, oceanography, ecology and environmental management (Creutin and Obled 1982, Bilonick 1988, Cambardlla *et al.* 1994, Merino *et al.* 2001, Kumar and Ahmaed 2003).

However, the GHG concentrations above a continent depend on many factors such as weather systems and terrestrial vegetation. And some errors related with satellite retrievals and atmospheric transport models. (Alkhaled *et al.* 2008). Therefore, this paper assumes that the distribution of the GHG fluxes ignores these impacts. A combination of ground monitoring data was used to verify the feasibility of this approach and will provide a basic understanding of the accuracy of the GOSAT data.

2. Study area and used data

2.1 Regional climate

The study region is located in eastern Asia on its Pacific coast. It stretches from 10° N to 50° N latitude and from 65° E to 150° E longitude. A broad range of climatological and geographical features exist within this region. Based on temperature and precipitation, the region can be roughly divided into three climate zones: arid and semi–arid, temperate and tropical (Preston *et al.* 2006). A combination of land classification maps (see figure 1) show that the arid and semi–arid region is composed of the northern extent of India and Pakistan as well as Mongolia and western China, and the landscape is composed of tropical savannah vegetation, grasslands, and desert (Shi *et al.* 2002). The temperate region is composed of the Tibetan Plateau, eastern China, Japan and the Korean Peninsula (Ren 1998). This landscape has been significantly altered due to centuries of deforestation and agriculture (Zhao *et al.* 2004). The tropical region is composed of central and southern India, Sri Lanka, Bhutan, Bangladesh, and Southeast Asia (i.e. Myanmar, Vietnam, Laos, Cambodia, and Thailand) (Preston *et al.* 2006). These subregions are geographically diverse and contain a number of hotspots for terrestrial and marine biodiversity.

As the latitude of this study region has a large span, the temperature and precipitation show wide variations. For example: north of 30°N latitude, temperatures in January may be at or below freezing, particularly in the high altitude areas around the Himalayas. In contrast, the tropical areas south of 30°N, such as the Indian subcontinent, Southeast Asia, Indonesia, and the

Pacific Islands, generally experience temperatures above 25°C throughout the year (IRI/LDEO Climate Data Library). Regional rainfall and, consequently, temperature are strongly influenced by the summer and winter monsoons. The summer monsoon season influences the climate of this region from May to September and brings rain to South and Southeast Asia and east China. The northeast winter monsoon season controls the climate from December to February and is characterized by dry winds out of the northeast that bring significant rainfall to parts of Southeast Asia, but leave much of South Asia dry, particularly central and northern India. The two inter–monsoon or transitional seasons comprise March to April and October to November (Kawamura *et al.* 2004). Therefore, seasonal changes in this region occur during January, April, July, and October.

2.2 GOSAT XCO_2 and XCH_4 data

GOSAT monitors CO_2 and CH_4 globally from space using two instruments. The Thermal and Near Infrared Sensor for Carbon Observation Fourier–Transform Spectrometer (TANSO–FTS) detects the gas–absorption spectra of the solar SWIR reflected from the Earth's surface as well as of the thermal infrared radiated (TIR) from the ground and atmosphere. From the SWIR data, the column densities of CO_2 and CH_4 data are acquired, and from the TIR data, CO_2 vertical profiles are retrieved (Akihiko *et al*. 2009). Every three days, global GHG distributions are created, and by inversion with a chemical transfer model, sources and sinks of GHGs are finally retrieved. An initial retrieval of these gaseous concentrations was performed for measurement scenes of cloud–free conditions over land (Yokota *et al*. 2008, 2009).

XCO_2 is the ratio of the total number of CO_2 molecules to the total number of dry air molecules that exist not only close to the Earth's surface but also in the total vertical column from the surface up to the top of the atmosphere. The same definition applies for XCH_4. The data release of the FTS Level 2 XCO_2 and XCH_4 column abundance products to general users started on February 18, 2010, and newly collected data are released every month. Table 1 shows the relationship between observation period and version of the used FTS Level 2 SWIR data (GOSAT Project 2010).

2.3 Ground observation data

The WDCGG, one of the World Data Centres (WDC) under the World Meteorological Organization's (WMO's) Global Atmosphere Watch (GAW) programme, has been operating since October 1990 at the Japan Meteorological Agency (JMA). The WMO WDCGG data contains all the metadata and observational data from about 320 stations, which the WDCGG accepted by November 2009. Based on the GOSAT coverage period, two stations' monthly mean data were used as the ground verification point data in this region, and the stations were the Hong Kong Observatory (114.173° E, 22.312° N) and Yonaguni-jima island, Japan (123.02° E, 24.47° N) (see figure 2). The WDCGG website is http://gaw.kishou.go.jp/wdcgg/wdcgg.html.

3. Method

3.1 Data pre–processing

Based on the version 01.xx of the GOSAT Level 2 data products, extremely low or high values of Level 2 XCO_2 (lower than 360 ppm or higher than 390 ppm) and XCH_4 (lower than 1.60 ppm or higher than 1.90 ppm) are observed in some month in this region. In the Kriging interpolation, these data may have a significant impact on the interpolation result. So these extremely data are removed in the data pre–processing. This process also used in the Level 3 data processing, called 'screening' (NIES GOSAT Project 2011). The screening process is performed using skewness and kurtosis to remove these extreme values that make the Level 2

data distribution differ markedly from normal distribution. Next, monthly data were used for the analysis: as the GOSAT comes back to the same path every 3 days, there are many duplicate data at the same point in 1 month, with numbers of the duplicate data ranging from 2–5. Therefore, the mean value of these data was used. In addition, according to the algorithm theoretical basis document for GOSAT TANSO-FTS Level 3 data, the GHG distribution tendency varies a lot between land and sea due to the difference in their empirical variograms (NIES GOSAT Project 2011). So, we removed all the data over the ocean by using ArcGIS software. The spatial distribution of the samples of XCO_2 data in September 2009 is shown in figure 3, and, after treatment, the number of points was reduced from 1031 to 457. The histograms for these two data sets of original data and processed data are also given in the figure. According to this evidence, the two data sets were almost identical.

3.2 Kriging method application

The Kriging method, also known as space–local estimation or space–local interpolation, is a method of making linear, unbiased, optimal estimates of values of regionalized variables for un–sampled points by using the means of the original data of the regionalized variables and the structural features of semi–variogram (Kumar and Remadevi 2006). Although details on the Kriging techniques are well documented (Journel and Huijbregts 1978), a brief introduction of the relevant methods used is given below.

The important step in Kriging is the variogram analysis, which consists of calculating the experimental variogram and fitting the variogram model to the data (Kushavand *et al*. 2007). The experimental variogram is calculated by using the following equation:

$$\gamma(h) = \frac{1}{2N(h)} \sum_{i=1}^{n} [Z(x_i) - Z(x_i + h)]^2 \tag{1}$$

Where $\gamma(h)$ is the estimated value of the semi–variogram for the lag of h; n is the number; $N(h)$ is the number of experimental pairs separated by vector h; $Z(x_i)$ and $Z(x_i + h)$ are the values of the variable Z at x_i and $x_i + h$, respectively, and x_i and $x_i + h$ are the positions in two dimensions.

The variogram model, with minimum standard error is chosen from various theoretical models such as the spherical, exponential, gaussian, linear and rational quadratic. The appropriate model is chosen by the experimental variogram fitted to the theoretical model.

A variogram represents both structural and random aspects of the data under consideration. A Spherical and Gaussian variogram model fitting to the experimental variogram data were used as an example to discuss the analysis process (see figure 4). The variogram values increase with increases in the distance of separation until it reaches the maximum (C) at a distance known as the "range" (A). If at a distance nearly equal to 0, the variogram value is greater than 0, this value is known as the "nugget–effect" (C_0). The total–sill of the variogram (S) is $C_0 + C$. Often, C is also treated equal to the sill of the variogram model fitted to the experimental variograms and C_0. Both C_0 and the S characterize the random aspect of the data, whereas the A and C characterize the structural aspect of the data.

The first step of a variogram analysis is to model and review the omnidirectional variogram to infer the sill of the anisotropic variograms. The total sill of an omnidirectional variogram provides an approximation of the total sill of the specific directional variograms. So, we adjusted the parameters of the experimental model to achieve the appropriate degree of model simulation. The sill, and the nugget effect were chosen based upon the omnidirectional variogram.

The second major aspect of directional variogram modelling is examination of the anisotropy of the variable. The experimental variogram shows different length scales in different directions.

When modelling the variogram anisotropy, an anisotropic set of variograms should be fitted to the experimental variogram. If the sills of the variograms are comparable, but the ranges of the variograms change with direction, a variogram with components of the "geometric anisotropy" type should be fitted to the experimental variogram.

The quality of the Kriging predictions were examined on the basis of the cross–validation results and on the basis of a Kriging variogram analysis.

4. Results and discussion

For data analysis, the variogram analysis, model fitting, Kriging interpolation and surface output were performed with the ArcGIS 9.3.1, GS+ for Windows 9.0 and Surfer 9.0 software applications.

4.1 Statistics of the processed Level 2 data

According to the data pre–processing methods, 12 monthly data set from June 2009 to May 2010 were processed .

From the processed results, we can see that the spatial distribution of the points and the numbers varies monthly (see figure 5). The reason of the retrieved area's change is considered that the retrieval process accomplishes the creation of Level 2 data based on TANSO–FTS Level 1B data, which includes the pre–process, the data screening process, the retrieval process and the quality check process. Only the data that pass the quality check should be distributed to the public as a final data (NIES GOSAT Project 2010). .

Basic statistics of the data analysis are shown in tables 2 and 3. The processed value of XCO_2 and XCH_4 data were in the range of 360–400 ppm and 1.60–1.90 ppm respectively; the monthly standard deviation values were also relatively small. From the monthly trend of the mean values of the XCO_2 the data was lower in September and October, but higher in March and April. Respectively, the mean values of XCH_4 was trends lower in April, May and June, but higher from August to January. The seasonal variation is observed, but it needs a long time monitoring verification.

The statistical analyses use skewness and kurtosis to characterize the location and variability of a data set. Skew is the degree of departure from the symmetry of a distribution. Kurtosis is the degree of 'peakedness' of a distribution. From tables 2 and 3, all the data conformed to a normal distribution (see figures 6 and 7).

4.2 Variogram analysis and theoretical model of the processed Level 2 data

All the data were analysed to obtain the various fitting parameters for each model. The method for fitting models was to (1) analyse the data for all months with the variogram analysis module in GS+ for Windows software; (2) select the model with the root mean square standardized closest to 1 and the minimum residual sum of Downloaded by squares (RSS); and (3) obtain the various fitting parameters for each model in Surfer software. Finally, the model parameters were corrected by cross validation. The variogram models and related parameters for all the data are shown in tables 4 and 5. For all the XCO_2 data, a Gaussian model resulted in a minimum standard error and was thus considered to be the best-fitting model for October and November 2009, and February 2010; others were using the spherical model (see table 4). For the XCH_4 data sets, a Gaussian model fitted well with the data for October, November and December 2009, and January and February 2010, whereas for the other data, a spherical model gave a better fit (see table 5).

Distinct classes of spatial dependence were obtained by the ratio of the nugget to sill ($C_0/(C_0+C)$). If the ratio was $< 25\%$, between 25 and 75% or $> 75\%$, the variable was considered strongly, moderately or weakly spatially dependent, respectively (Cambardlla *et al.*

1994). In table 4, all of the values of $C_0/(C_0+C)$ for the XCO$_2$ data are below 50%, which indicated that the degree of spatial dependence was moderate, especially for July 2009 (10%), which were very strong. In table 5, the data show that the values of $C_0/(C_0+C)$ for XCH$_4$ were between 25% and 50% in August 2009, February, March and May 2010 (29%, 33%, 47% and 31%, respectively), so the degree of spatial dependence was moderate. Others were strongly spatial dependent.

The nugget effect (C_0) represents the variation caused by experimental errors and processes that occur on a scale smaller than the experimental sampling scale. The C_0 of the XCO$_2$ data was small for July 2009 (3.6) but large for April and May 2010 (20.0 and 28.0 respectively). In contrast, the C_0 values for all of the XCH$_4$ data were small and less variable (table 5).

A large spatial range (A) indicates that the spatial distribution of the research object in the area is more irregular. When comparing the results across months, the range of XCO$_2$ for November, December 2009 and January 2010 was big (30.0 km, 36.0 km and 30.0 km respectively), and the ranges of XCH$_4$ for October, November, December 2009 and January 2010 were large (34.0 km, 26.0 km 30.0 km and 33.0 km, respectively), which means that the regularity of the spatial distribution of the data in these months was not strong. Therefore it is possible that range be related not to the spatial variation but to the temporal variation.

A coefficient of determination (R^2) close to 1 means that the curve is smooth and the fit of the model is very good. For the XCO$_2$ and XCH$_4$ models, only the R^2 value of the XCH$_4$ data for April 2010 has less R^2 (0.73). The models for the other data fit the data quite well.

The RSS is a measure of the discrepancy between the data and an estimation model. A small RSS indicates a tight fit of the model to the data. For XCO$_2$ result, the RSS was very small in October 2009, January and March 2010 (5.3, 3.2 and 7.7 respectively). All RSS for the XCH$_4$ data was small.

The experimental variograms and the best–fitted theoretical model for all the data are shown in figures 8 and 9. And the best anisotropic set of variograms fitted to each experimental variogram are also shown in the figures.

4.3 Kriging interpolation

In accordance with the variance functional models obtained by adopting the Kriging method for optimal interpolation, the Surfer software was used to draw contour maps of XCO$_2$ and XCH$_4$ and estimate variances. All the images were made with the same classification instructions. For the images of the interpolation results, the seasonal results, which include summer (June, July and August 2009); autumn (September, October and November 2009); winter (December 2009, January and February 2010); spring (March, April and May 2010), are shown in figures 10 and 11. According to the seasonal changes, the XCO$_2$ concentrations were higher in winter and spring (figures 10 (*h-k*)) and lower in summer and autumn (figures 10 (*b-e*)). This phenomenon may be due to smoke and dust because the majority of the developing countries in this region depend on coal for heating in winter.

The XCH$_4$ distribution changes were obviously affected by latitude in autumn and winter (figures 11 (*d*), (*e*), (*f*), (*g*), (*h*) and (*i*)). The XCH$_4$ concentration was high south of 30°N latitude but low north of 30°N latitude. This may be mainly affected by temperature because in this area, the temperature of most of the region is below freezing in the area north of 30°N latitude, but in the area south of 30°N latitude, the temperature is between 0 ˚C and 25 ˚C. In summer and spring (figures 11 (*a*), (*b*), (*c*), (*j*), (*k*) and (*l*)), the distribution of XCH$_4$ concentrations was more uniform.

4.4 Verification with the ground observation stations

The results of the comparison of the Kriging values and the observation data are shown in figure

12. Overall, the Level 2 Kriging interpolation values were lower. In Hong Kong and Japan where the two observation stations are, the monthly average XCO_2 Kriging interpolation data were lower than the ground observation data of by 4.8% and 2.2%, respectively (figures 12 (*a*) and (*b*)). The average XCH_4 Kriging interpolation data were lower than the ground observation data by 4.2% (figure 12 (*c*)). According to the verification results in the FTS SWIR Level 2 (V01.XX) product, which was provided by the GOSAT project, the average concentration of XCO_2 and XCH_4 were approximately lower than the validation data by 2–3% and 1–2%, respectively (NIES GOSAT Project 2010).

From the monthly data, The XCO_2 data and ground observation data were more consistent well. However, in some of the months, the Kriging interpolation values had some different. This may be due to the smaller number of samples in this region during these months, which resulted in the inaccurate interpolation results. However, the XCH_4 interpolation results were inconsistent with the observational data. The reasons may be that there was smaller distribution of samples in this region.

4.5 Comparison with FTS Level 3 data

The FTS SWIR global Level 3 products were released to the GOSAT project users on 28 October 2010. So, the XCO_2 and XCH_4 FTS Level 3 data from September 2009 were compared with the FTS Level 2 Kriging interpolation data as an example to evaluate the accuracy. The results are shown in figure 13. Overall, the spatial resolution of Level 3 map is about 2˚. In contrast, the spatial resolution of Level 2 Kriging interpolation map is about 0.8˚. And there are some blank areas in the Level 3 data. Two compared images were made with the same classification instructions. From the concentration distribution map, the interpolation results were consistent with Level 3 data, excluding individual areas such as XCO_2 in the part of east China and XCH_4 for south Japan. Therefore, it is possible because of the FTS Level 2 data has some lower concentration data than FTS Level 3 data (XCO_2 and XCH_4 values lower than 370 ppm and 1.74 ppm, respectively).

5. Conclusion

In this article, the Kriging method was applied to map the spatial distribution of XCO_2 and XCH_4 data obtained from the GOSAT. The data used included 12 months between June 2009 and May 2010. The results reached are described below.

GOSAT data can be used effectively as reference data for monitoring atmospheric GHG concentrations on a regional scale. The FTS Level 2 data will continue to update in the future, and also the FTS Level 3 data is produced to the users. This article used Kriging method to estimate the distribution of GHG concentrations over the land throughout the studied region. The parameters for the variogram model changed with the different months and fitted well for their corresponding variogram models. According to the Kriging interpolation map, the concentration of XCO_2 was higher in winter and spring, which may be caused by smoke and dust from coal combustion. The concentration of XCH_4 changed significantly with latitude and was mainly affected by temperature. In addition, from the verification of the results, the FTS Level 2 Kriging interpolation values were lower than the ground observation data, and consistent with FTS global Level 3 data without the individual areas of low concentration.

There are several GIS software used in Kriging interpolation analysis. In this paper the Kriging method was evaluated based on Surfer and GS+ for windows. It provided convenient data screening and produced results with the smallest RSS and highest correlation of determination. This analysis is recommended to interpolate data and generate a map in a regional scale. In the future, with long time monitoring and comparison with other similar satellite data, it will be possible to verify the feasibility of this approach and examine the accuracy of the GOSAT data.

Acknowledgments

References

AKIHIKO, K., HIROSHI, S., MASAKATSU, N. and TAKASHI, H., 2009, Thermal and near infrared sensor for carbon observation Fourier–transform spectrometer on the Greenhouse Gases Observing Satellite for greenhouse gases monitoring. *Applied Optics*, **48**, pp. 6716–6733.

ALKHALED, A.A., MICHALAK, A.M. and KAWA, S.R., 2008, Using CO_2 spatial variability to quantify representation errors of satellite CO_2 retrievals. *Geophysical Research Letters*, **35**, L16813, doi:10.1029/2008GL034528.

BILONICK, R.A., 1988, Monthly hydrogen ion deposition maps for the North Eastern US from July 1982 to Sept.1984. *Atmospheric Environment*, **22**, pp. 1909–1924.

BUCHWITZ, M., BEEK, R., BURROWS, J.P., BOVENSMANN, H., WARNEKE, T., NOTHOLT, J., MEIRINK, J.F., GOEDE, A.P.H., BERGAMASCHI, P., KORNER, S., HEIMANN, M. and SCHULZ, A., 2005, Atmospheric methane and carbon dioxide from SCIAMACHY satellite data: Initial comparison with chemistry and transport models. *Atmospheric Chemistry and Physics*, **5**, pp. 941–962.

BUCHWITZ, M., SCHNEISING, O., BURROWS, J.P., BOVENSMANN, H. and NOTHOLT. J., 2007, First direct observation of the atmospheric CO_2 year–to–year increase from space. *Atmospheric Chemistry and Physics*, **7**, pp. 6719–6735.

CAMBARDLLA, C.A., MOORMAN, T.B., NOVAK, J.M., PARKIN, T.B., KARLAN, D.L., TURCP, R. F. and KONOPKA, A.E., 1994, Field scale variability of soil properties in central Iowa soils. *Soil Science Society of America Journal*, **58**, pp. 1501–1511.

CRACKNELL, A.P. and VAROTSOS, C., 2007, Editorial –Fifty years after the first artificial satellite: from Sputnik 1 to ENVISAT. *International Journal of Remote Sensing*, **28**, pp. 2071–2072.

CREUTIN, J.D. and OBLED, C., 1982, Objective analysis and mapping techniques for rainfall fields: An objective comparison. *Water Resources Research*, **18**, pp. 413–431.

GOSAT PROJECT, 2010, Remarks on the Use of the FTS SWIR Level 2 Data Product (V01.xx). GOSAT User Interface Gateway. Available online at: http://www.gosat.nies.go.jp/index.html (accessed 10 February 2010).

IPCC FAQ 7.1., 2007, Climate Change 2007: Working Group *I*: The Physical Science Basis, IPCC Fourth Assessment Report. Available online at: http://www.ipcc.ch/publications_and_data/ar4/wg1/en/faq-7-1.html

IRI/LDEO Climate Data Library, 2010, the monthly surface air temperature climatology (deg. C) for 1961–1990 on a 0.5×0.5 deg. lat/lon grid. Climatology data were derived from the Climate Research Unit of the University of East Anglia. Available online at: http://iridl.ldeo.columbia.edu/maproom/Global/.Climatologies/.Temp_Loop.html.

JOURNEL, A.G. and HUIJBREGTS, C.J., 1978, *Mining Geostatistics*, 600pp. (London: Academic Press).

KAWAMURA, R., SUPPIAH, R., COLLIER, M.A. and GORDON, H.B., 2004, Lagged relationships between ENSO and the Asian Summer Monsoon in the CSIRO coupled model.

Geophysical Research Letters, **31**, doi:10.1029/2004GL021411.

KONDRATYEV, K.Y. and VAROTSOS, C., 1995, Atmospheric greenhouse effect in the context of global climate change. *Nuovo Cimento Della Societa Italiana di Fisica C–Geophysics and Space Physics*, **18**, pp. 123–151.

KUMAR, D. and AHMAED, S., 2003, Seasonal behavior of spatial variability of groundwater level in a granitic aquifer in monsoon climate. *Current Science*, **84**, pp. 188–196.

KUMAR, V. and REMADEVI., 2006, Kriging of Groundwater Levels – A case study. *Journal of Spatial Hydrology*, **6**, pp. 81–94.

KUSHAVAND, B., AGHABABEI, H. and ALIZADEH, B., 2007, Application of Kriging with Omni Directional Variogram to Finding the Direction of Anisotropy Axes. *Journal of Applied Sciences*, **7**, pp. 589–592.

MERINO, G.G., JONES, D., STOOKSBURY, D.E. and HUBBARD, K.G., 2001, Determination of semivariogram models to krige hourly and daily solar irradiance in Western Nebraska. *Journal of Applied Meteorology*, **40**, pp. 1085–1094.

NIES GOSAT Project, 2010, Algorithm theoretical basis document for CO_2 and CH_4 columun amounts retrieval from GOSAT TANSO–FTS SWIR, NIES–GOSAT–PO–014, V1.0.

NIES GOSAT Project, 2011, Algorithm theoretical basis document for GOSAT TANSO–FTS L3, NIES–GOSAT–PO–017, V1.0.

PRESTON, B., SUPPIAH, R., MACADAM, I. and BATHOLS, J., 2006, Climate Change in the Asia Pacific region. A consultancy report prepared for the Climate Change and Development Roundtable. *CSIRO Marine and Atmospheric Research*, pp. 13–20.

REN, G., 1998. Temperature changes of the 20th century over Horqin region, Northeast China. *Scientia Meteorologica Sinica*, **18**, pp. 373–380.

SHI, Y. F., SHEN Y.P., and HU R.J., 2002. Preliminary study on signal, impact and foreground of climatic shift from warm–dry to warm–humid in Northwest China, *Journal of Glaciology Geocryology,* **24**, pp.219–226.

VAROTSOS, C., 2002, Climate change problems and carbon dioxide emissions: Expecting 'Rio+10' Global summit on sustainable development in Johannesburg (26th August–6th September 2002). *Environmental Science and Pollution Research*, **9**, pp. 97–98.

VAROTSOS, C., ASSIMAKOPOULOS, M.N. and EFSTATHIOU, M., 2007, Technical Note: Long–term memory effect in the atmospheric CO_2 concentration at Mauna Loa. *Atmospheric Chemistry and Physics*, **7**, pp. 629–634.

YOKOTA, T., OGUMA, H., MORINO, I. and INOUE, G., 2004, A nadir looking SWIR FTS to monitor CO_2 column density for Japanese GOSAT project, In Proceedings of the Twenty–Fourth International Symposium on space Technology and Science (Selected Papers), *JSASS and Organizing Communication of the 24th ISTS*, pp. 887–889.

YOKOTA, T., AOKI, T., EGUCHI, N., OTA, Y., YOSHIDA, Y., OSHCHEPKOV, S., BRIL, A., DESBIENS, R. and MORINO, I., 2008, Date retrieval algorithms of the SWIR bands of the TANSO–FTS Sensor aboard GOSAT. *Journal of Remote Sensing Society of Japan*, **28**, pp. 133–142.

YOKOTA, T., YOSHIDA, Y., EGUCHI, N., OTA, Y., TANAKA, T., WATANABE, H. and MAKSYUTOV, S., 2009, Global concentrations of CO_2 and CH_4 retrieved from GOSAT: First Preliminary Results. *Scientific Online Letters on the Atmosphere*, **5**, pp. 160–163.

ZHAO, L., PING, C.L., YANG, D., CHENG, G., DING, Y., and LIU, S., 2004. Changes of climate and seasonally frozen ground over the past 30 years in Qinghai–Xizang (Tibetan) Plateau, China. Global and Planetary Change, **43**, pp.19–31.

Tables

Table 1. The observation period for which FTS Level 2 data are available.

Year	Month	Data	Version
2009	Jun.	3-30	V01.10
	Jul.	1-31	V01.10
	Aug.	1-31	V01.20
	Sep.	1-30	V01.20
	Oct.	1-28	V01.30
		29-31	V01.10
	Nov.	1-30	V01.10
	Dec.	1-31	V01.10
2010	Jan.	1-31	V01.10
	Feb.	1-7	V01.10
		8-28	V01.20
	Mar.	1-15	V01.20
		16-31	V01.30
	Apr.	1-30	V01.30
	May	1-31	V01.30

Table 2. Basic statistics of processed Level 2 XCO_2 data.

Data								
					XCO_2			
		No.	Min (ppm)	Max (ppm)	Mean (ppm)	Std. deviation	Skewness	Kurtosis
Year	Month							
2009	Jun.	228	360	392	375	6.70	- 0.18	- 0.38
	Jul.	194	360	396	374	6.82	0.08	- 0.39
	Aug.	335	360	398	373	6.36	0.34	0.21
	Sep.	457	360	389	373	5.09	0.02	0.12
	Oct.	598	360	386	373	3.81	0.16	- 0.05
	Nov.	462	360	390	375	4.63	- 0.25	0.59
	Dec.	351	363	390	377	4.09	- 0.54	1.60
2010	Jan.	478	362	389	378	3.80	- 0.50	1.74
	Feb.	449	366	399	379	4.80	0.78	1.65
	Mar.	602	361	400	379	5.57	0.13	1.14
	Apr.	612	360	400	379	6.49	- 0.33	0.75
	May	461	361	400	378	7.64	- 0.04	- 0.13

Table 3. Basic statistics of processed Level 2 XCH_4 data.

Data								
					XCH_4			
		No.	Min (ppm)	Max (ppm)	Mean (ppm)	Std. deviation	Skewness	Kurtosis
Year	Month							
2009	Jun.	250	1.61	1.84	1.75	0.04	- 0.62	0.16
	Jul.	223	1.60	1.89	1.76	0.04	- 0.75	1.51
	Aug.	348	1.63	1.90	1.78	0.05	0.16	0.20
	Sep.	468	1.69	1.87	1.78	0.04	0.27	- 0.46
	Oct.	607	1.60	1.90	1.77	0.04	0.23	0.14
	Nov.	467	1.66	1.87	1.77	0.04	- 0.29	- 0.27
	Dec.	352	1.66	1.84	1.77	0.03	- 0.71	0.12
2010	Jan.	488	1.70	1.87	1.78	0.03	- 0.21	0.16
	Feb.	456	1.67	1.90	1.77	0.04	0.04	0.78
	Mar.	634	1.61	1.89	1.77	0.04	0.01	0.92
	Apr.	653	1.61	1.88	1.75	0.04	- 0.11	0.20
	May	485	1.62	1.89	1.75	0.05	- 0.17	- 0.06

Table 4. Theoretical model and related parameters of the processed Level 2 XCO_2 data characteristics.

Data Year	Month	Variogram Model	C_0 [1]	C_0+C [2]	$C_0/(C_0+C)$	A [3]	R^2	Residual SS
2009	Jun.	Spherical	14.5	46.5	0.3	5.5	0.85	72.4
	Jul.	Spherical	3.6	48.1	0.1	8.0	0.91	52.5
	Aug.	Spherical	18.0	38.1	0.5	8.0	0.92	20.5
	Sep.	Spherical	13.5	26.9	0.5	17.0	0.94	11.3
	Oct.	Gaussian	8.3	18.1	0.5	25.5	0.99	5.3
	Nov.	Gaussian	12.3	27.3	0.5	30.0	0.96	15.3
	Dec.	Spherical	7.6	20.0	0.4	36.0	0.90	21.1
2010	Jan.	Spherical	8.4	16.4	0.5	30.0	0.96	3.2
	Feb.	Gaussian	16.8	32.3	0.5	14.0	0.97	20.9
	Mar.	Spherical	18.8	36.8	0.5	11.0	0.98	7.7
	Apr.	Spherical	20.0	48.0	0.4	7.5	0.86	74.0
	May	Spherical	28.0	63.0	0.4	6.5	0.88	78.7

[1]: Nugget effect   [2]: Structural Variance Sill   [3]: Range (km)

Table 5. Theoretical model and related parameters of the processed Level 2 XCH_4 data characteristics.

Data Year	Month	Variogram Model	C_0 [1]	C_0+C [2]	$C_0/(C_0+C)$	A [3]	R^2	Residual SS
2009	Jun.	Spherical	0.0003	0.0019	0.2	6.5	0.89	7.3E-08
	Jul.	Spherical	0.0005	0.0021	0.2	8.0	0.81	1.8E-07
	Aug.	Spherical	0.0007	0.0024	0.3	5.9	0.87	2.1E-07
	Sep.	Spherical	0.0005	0.0019	0.2	22.7	0.98	4.3E-08
	Oct.	Guasian	0.0002	0.0025	0.1	34.0	0.99	1.2E-07
	Nov.	Guasian	0.0004	0.0022	0.2	26.0	0.97	1.2E-07
	Dec.	Guasian	0.0002	0.0014	0.2	30.0	0.99	2.8E-08
2010	Jan.	Guasian	0.0003	0.0013	0.2	33.0	0.99	1.7E-08
	Feb.	Guasian	0.0004	0.0013	0.3	16.5	0.98	1.2E-08
	Mar.	Spherical	0.0007	0.0015	0.5	9.4	0.81	8.5E-08
	Apr.	Spherical	0.0004	0.0020	0.2	6.0	0.73	3.3E-07
	May	Spherical	0.0007	0.0021	0.3	7.4	0.91	1.0E-07

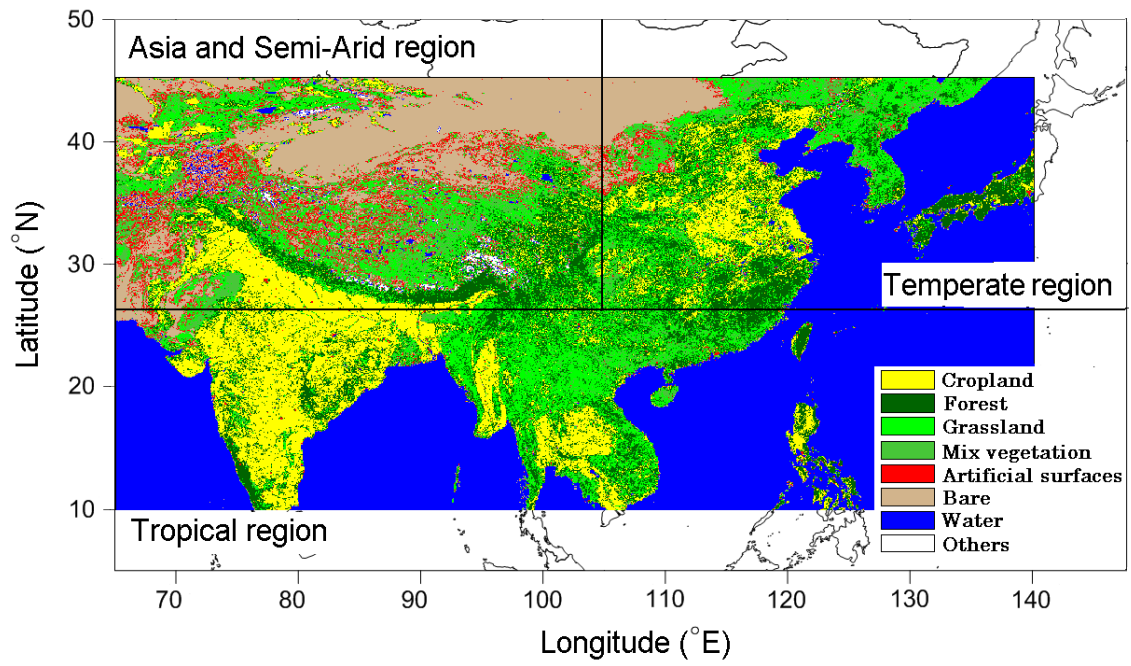[1]: Nugget effect   [2]: Structural Variance Sill   [3]: Range (km)

Figure 1. Land cover classification map and various subregions of East Asia derived from ESA (European Space Agency) global land cover data.
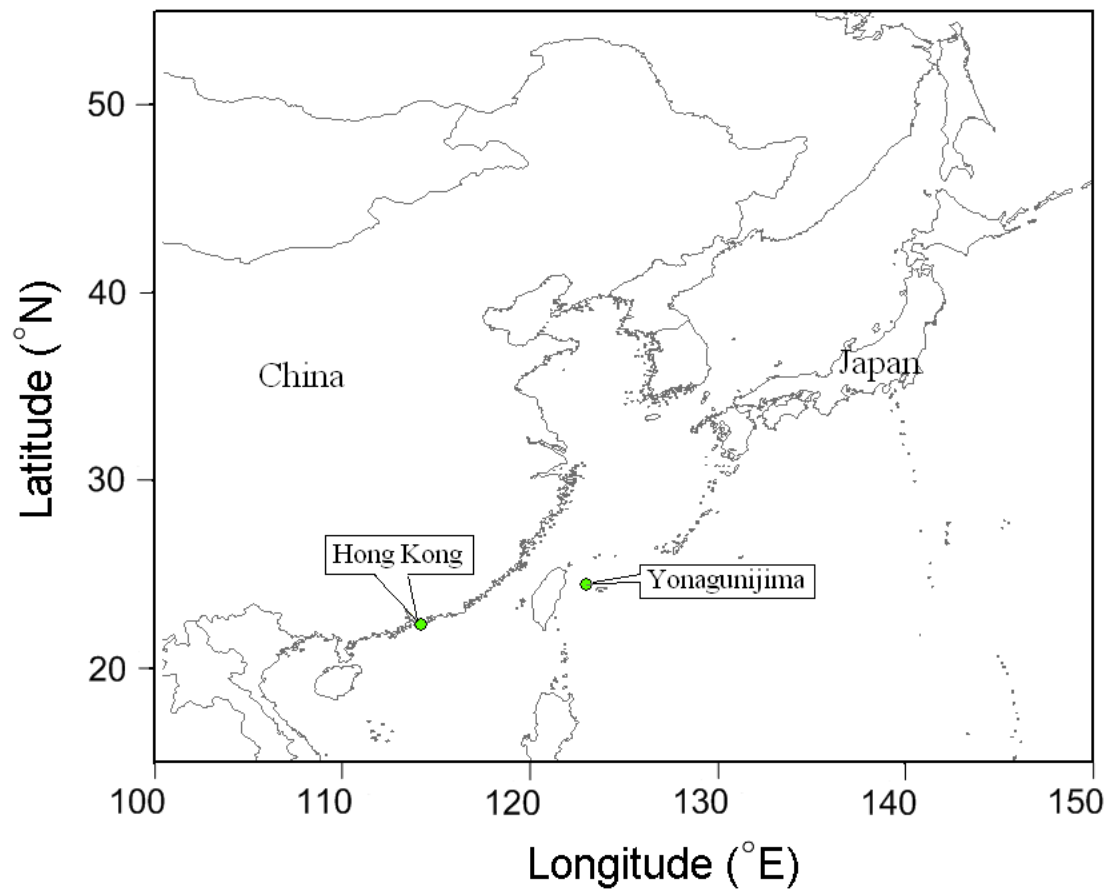
Figure 2. Location of WMO WDCGG data at the Hong Kong and Yonaguni-jima stations.
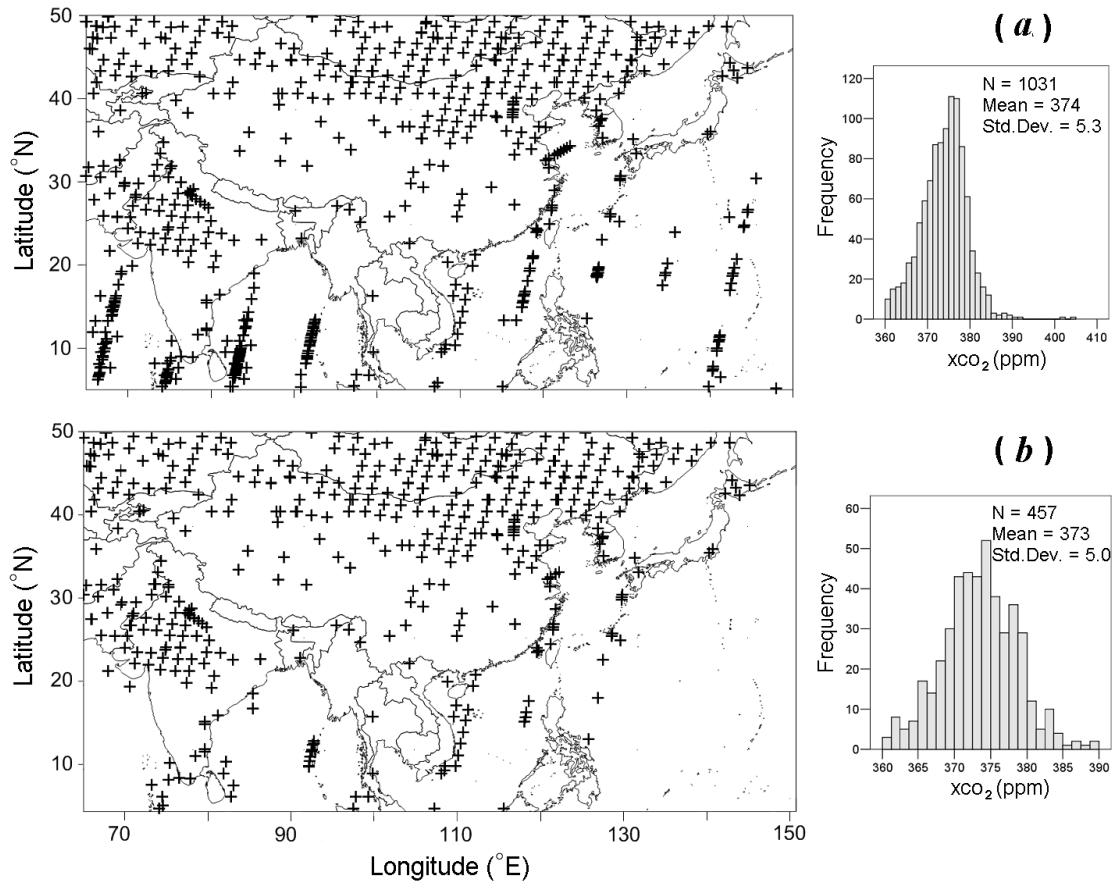
Figure 3. Distribution and histogram of samples of Level 2 XCO2 data in September 2009. (*a*)Original data, (*b*) processed data.
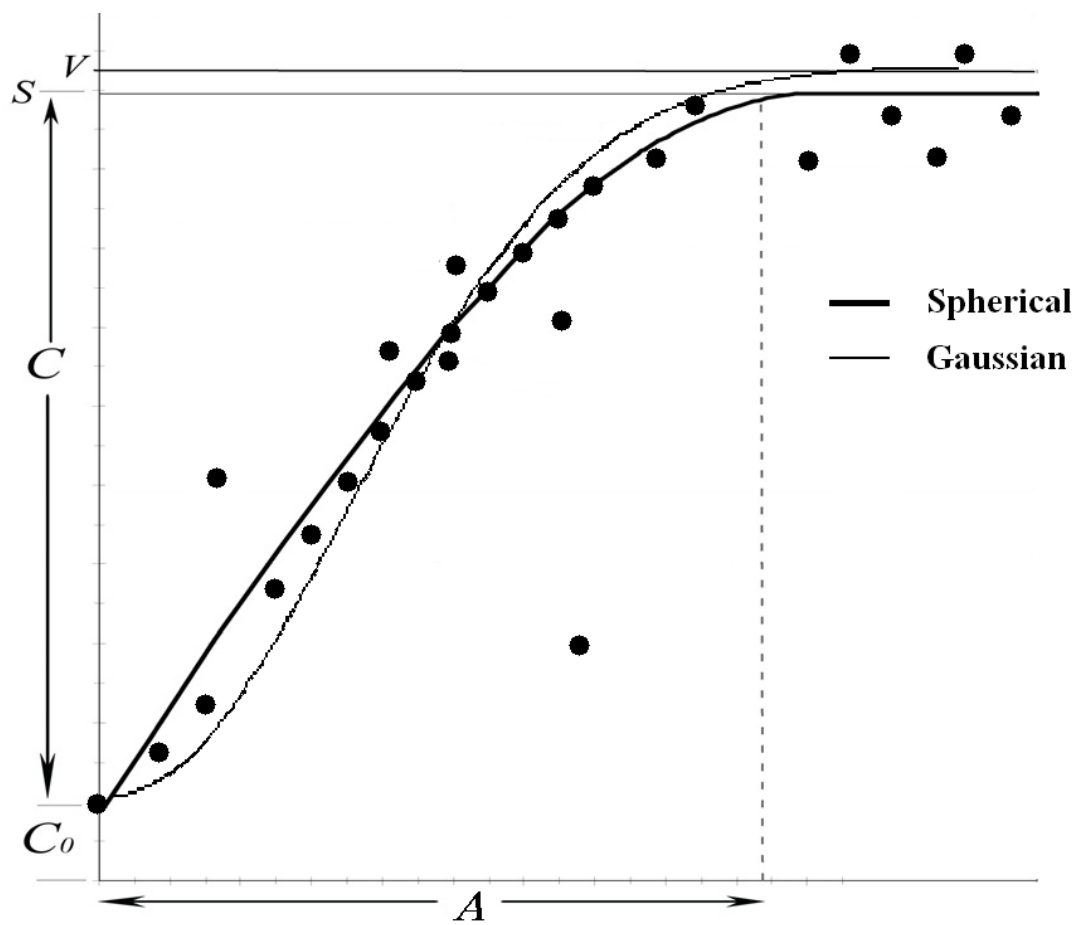
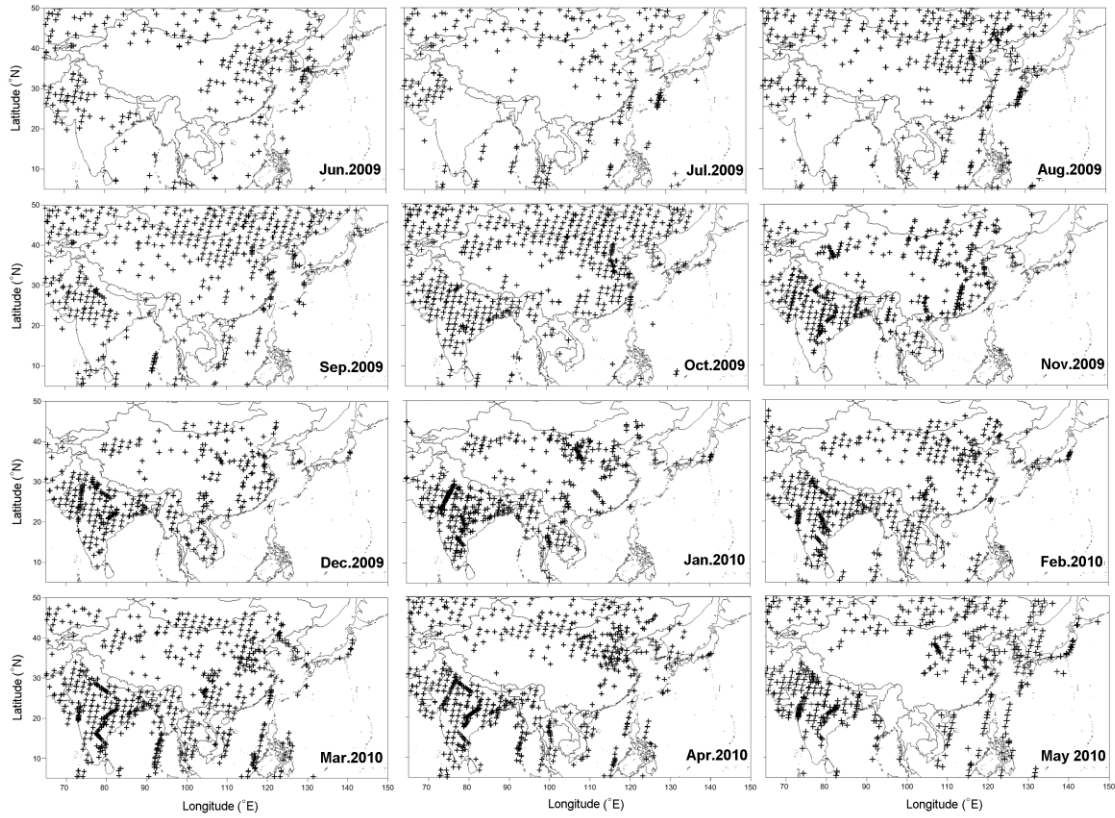Figure 4. Spherical and Gaussian variogram models fitted to the experimental variogram points.

Figure 5. Spatial distribution of processed Level 2 data from June 2009 to May 2010.
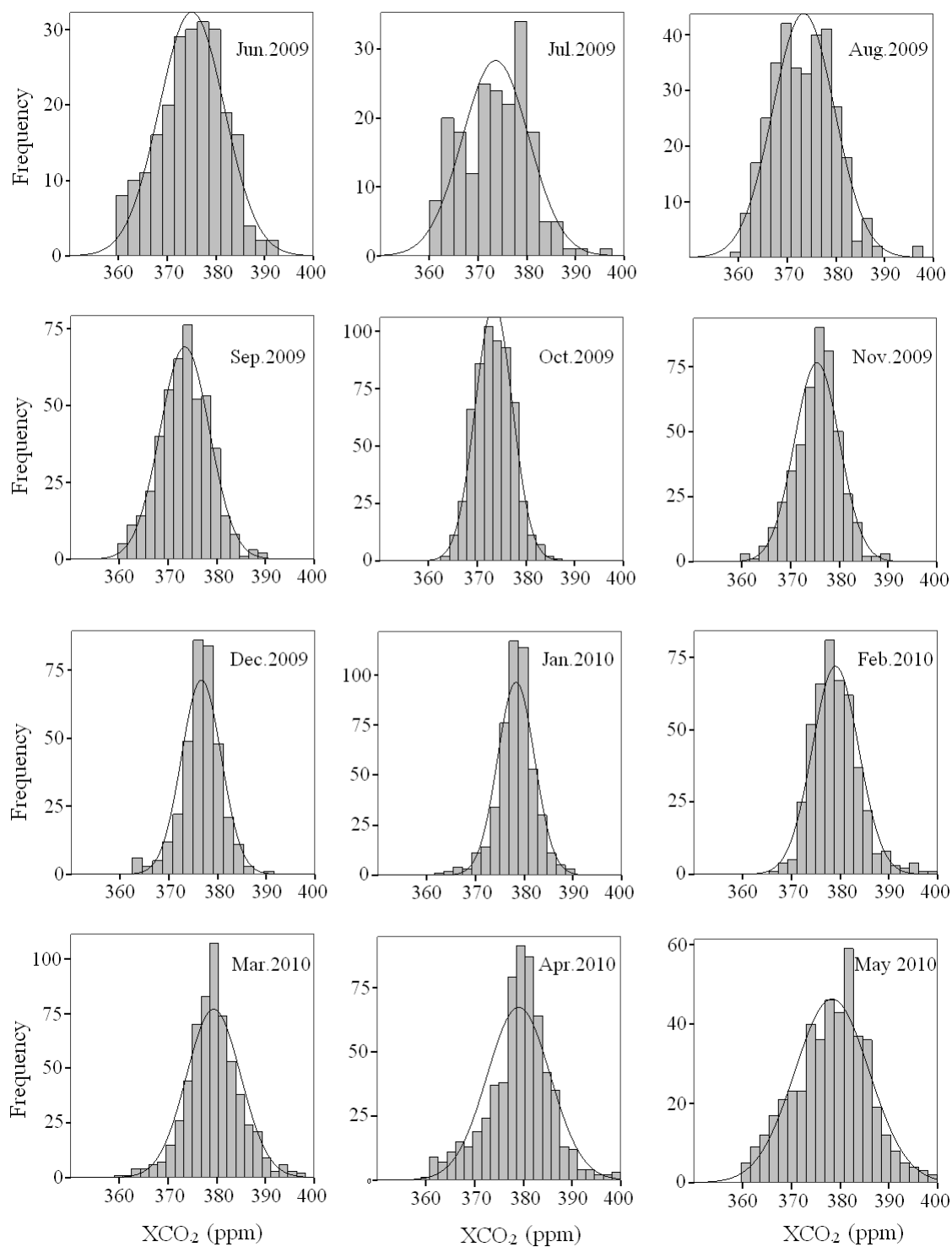
Figure 6. Normal distribution of processed Level 2 XCO_2 data from June 2009 to May 2010.
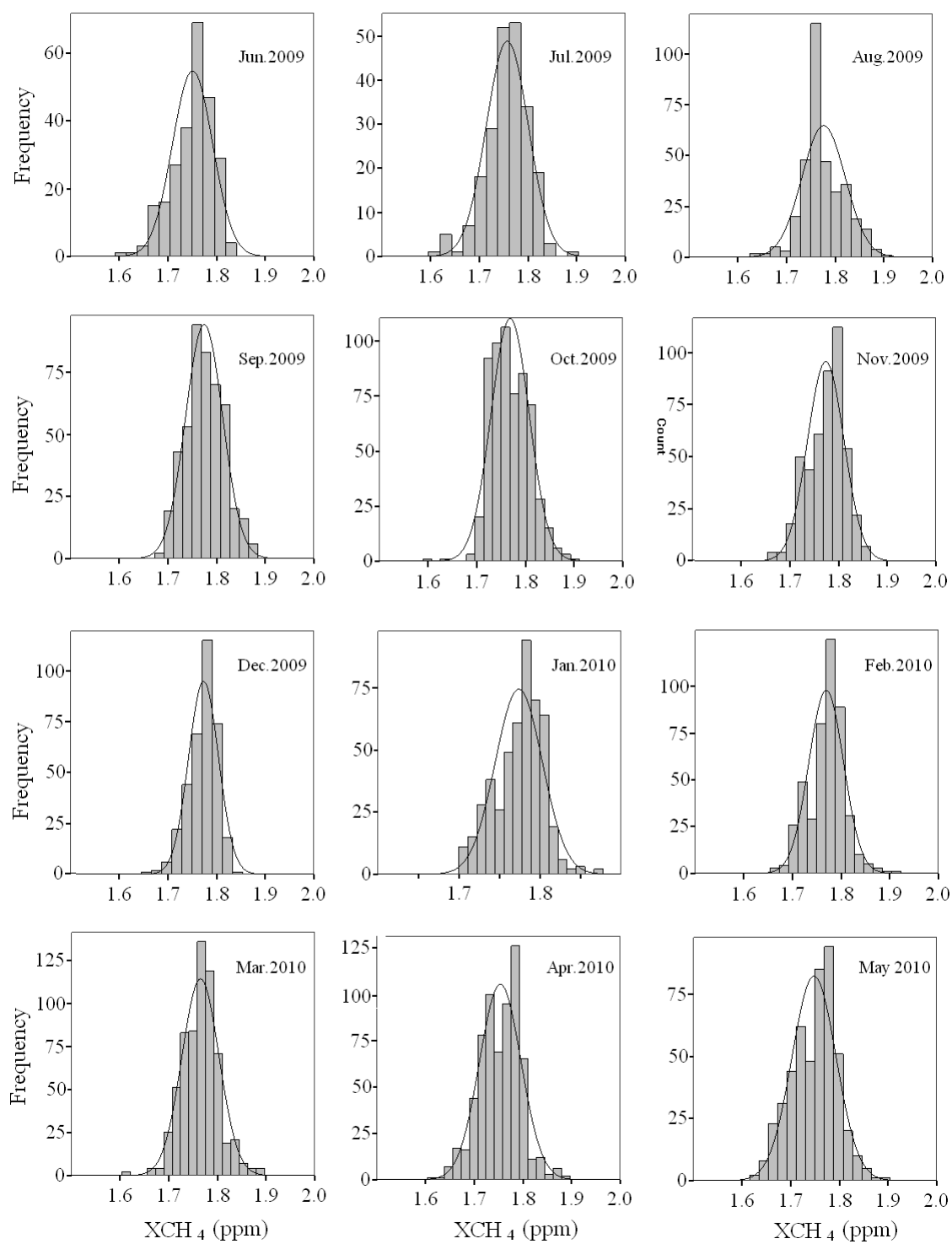
Figure 7. Normal distribution of processed Level 2 XCH_4 data from June 2009 to May 2010.
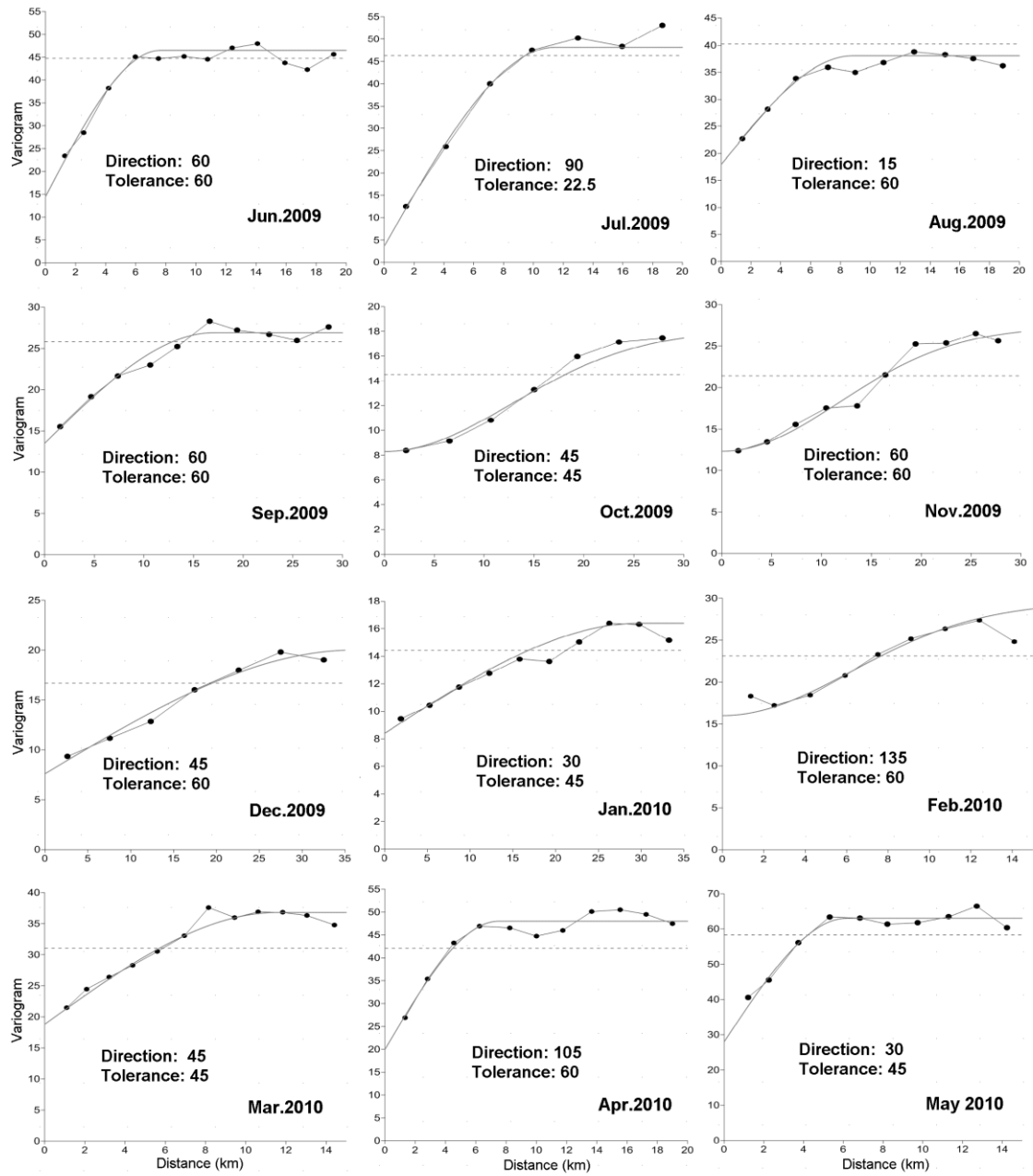
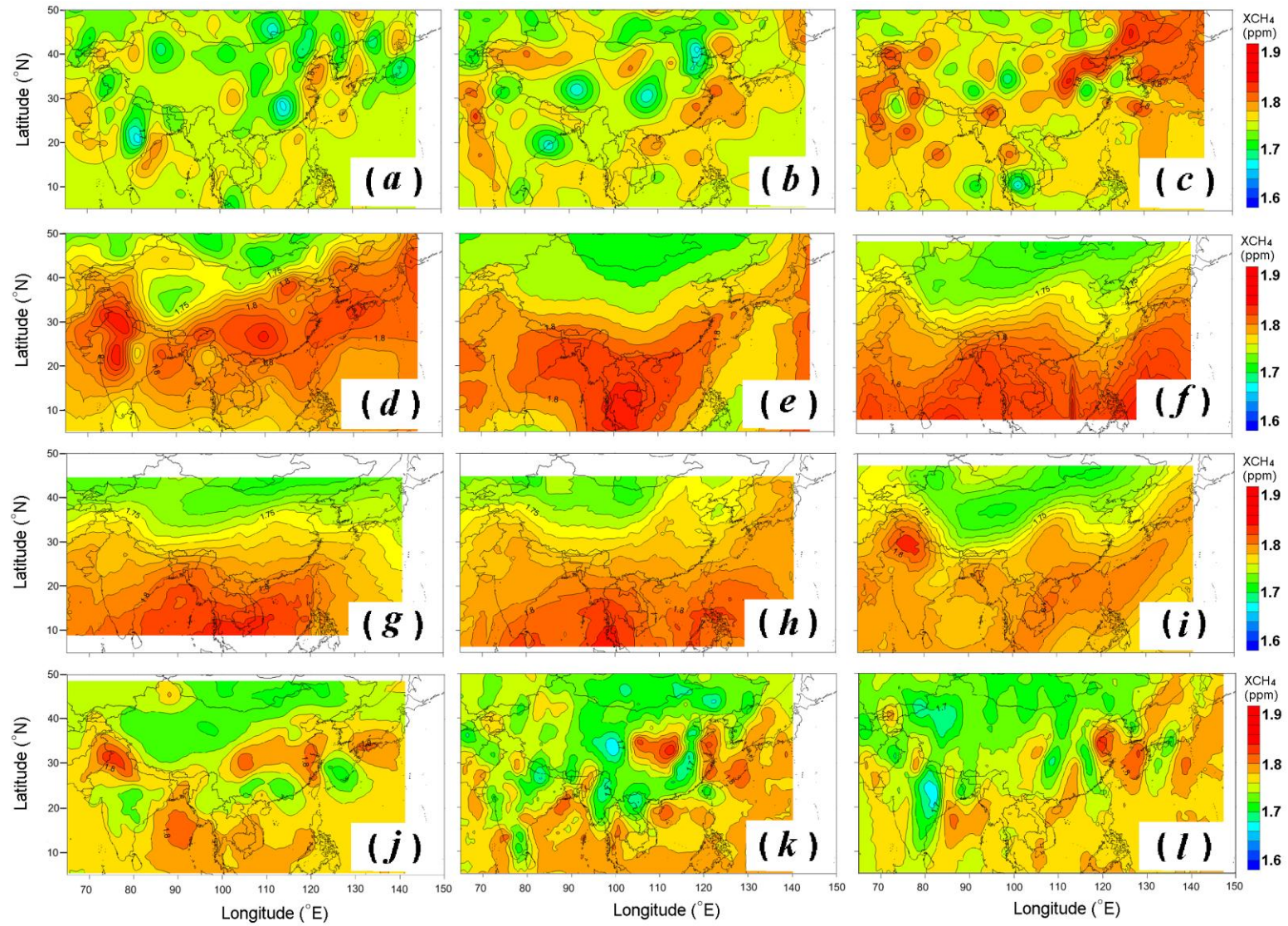Figure 8. Experimental and fitted variogram for XCO_2 data from June 2009 to May 2010.
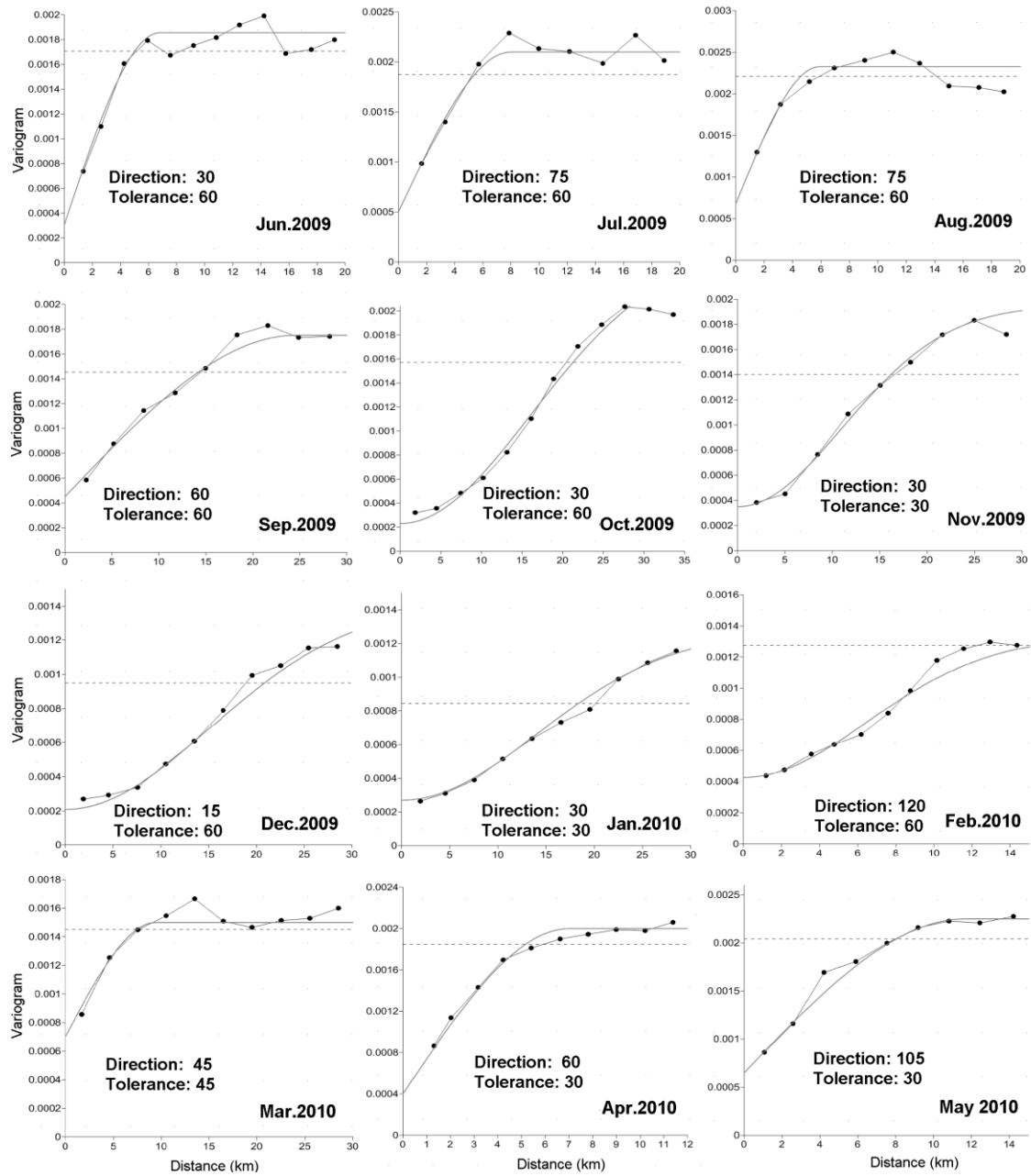
Figure 9. Experimental and fitted variogram for XCH_4 data from June 2009 to May 2010.

Figure 10. Kriging interpolation map of XCO_2 in the four seasons of summer (*a*) June 2009, (*b*) July 2009 and (*c*) August 2009; autumn (*d*) September 2009, (*e*) October 2009 and (*f*) November 2009; winter (*g*) December 2009, (*h*) January 2010 and (*i*) February 2010; and spring (*j*) March 2010, (*k*) April 2010 and (*l*) May 2010.
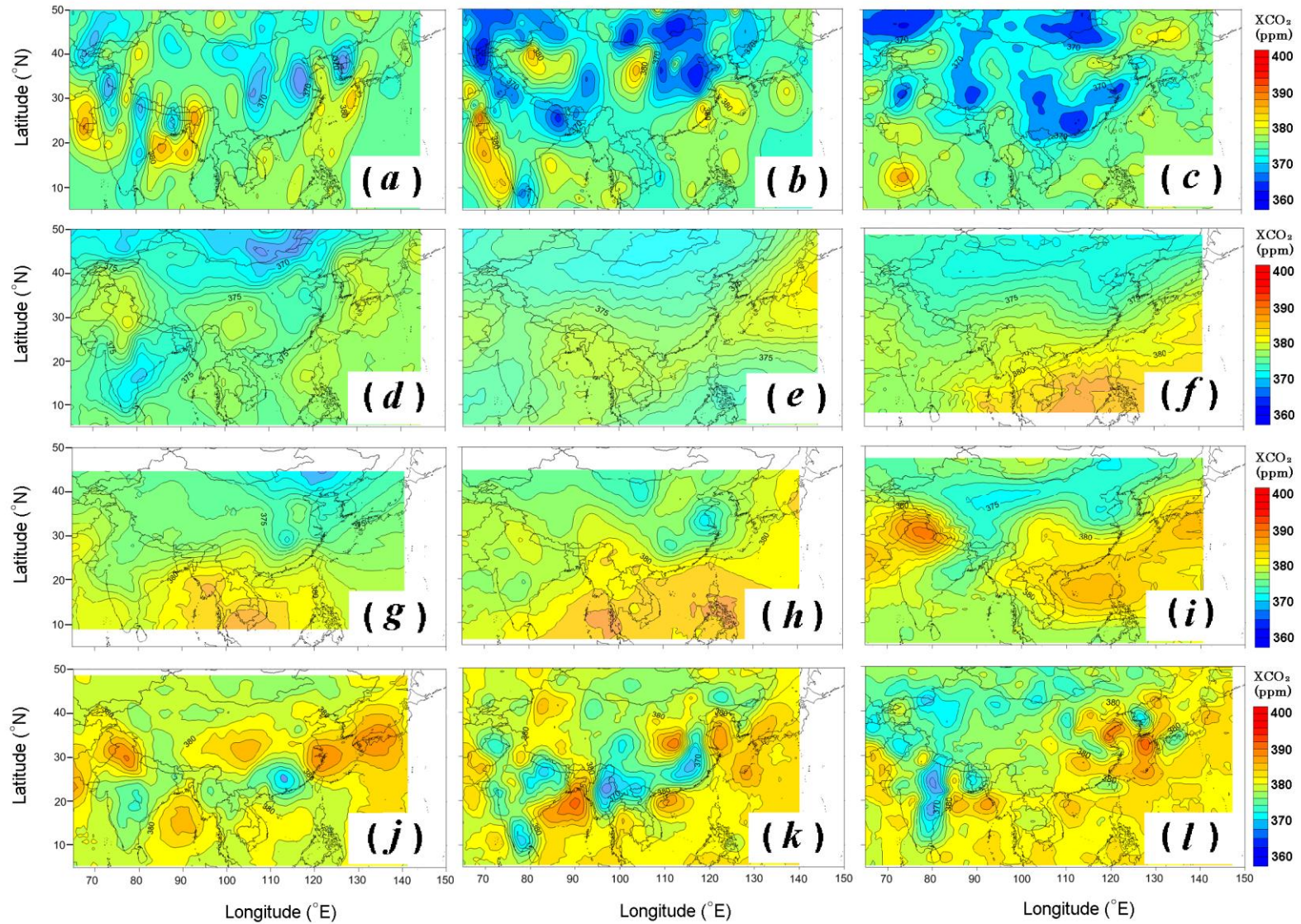
Figure 11. Kriging interpolation map of XCH$_4$ in the four seasons of summer (*a*) June 2009, (*b*) July 2009 and (*c*) August 2009; autumn (*d*) September 2009, (*e*) October 2009 and (*f*) November 2009; winter (*g*) December 2009, (*h*) January 2010 and (*i*) February 2010; and spring (*j*) March 2010, (*k*) April 2010 and (*l*) May 2010.
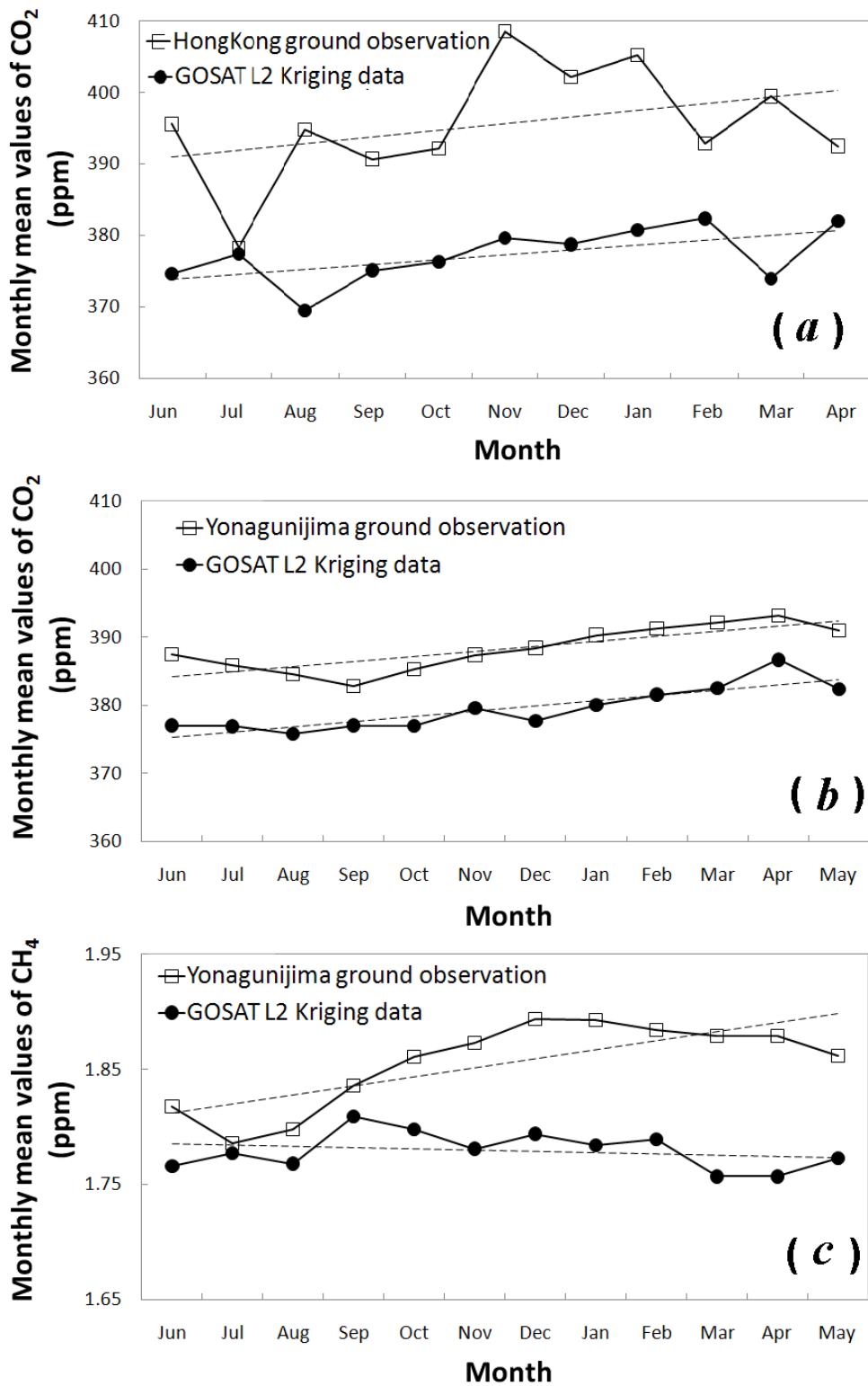
Figure 12. Monthly mean values of the Level 2 Kriging interpolation data and ground observation data: (*a*) XCO_2 in the Hong Kong site, (*b*) XCO_2 in the Yonaguni-jima site in Japan and (*c*) XCH_4 in the Yonaguni-jima site in Japan.
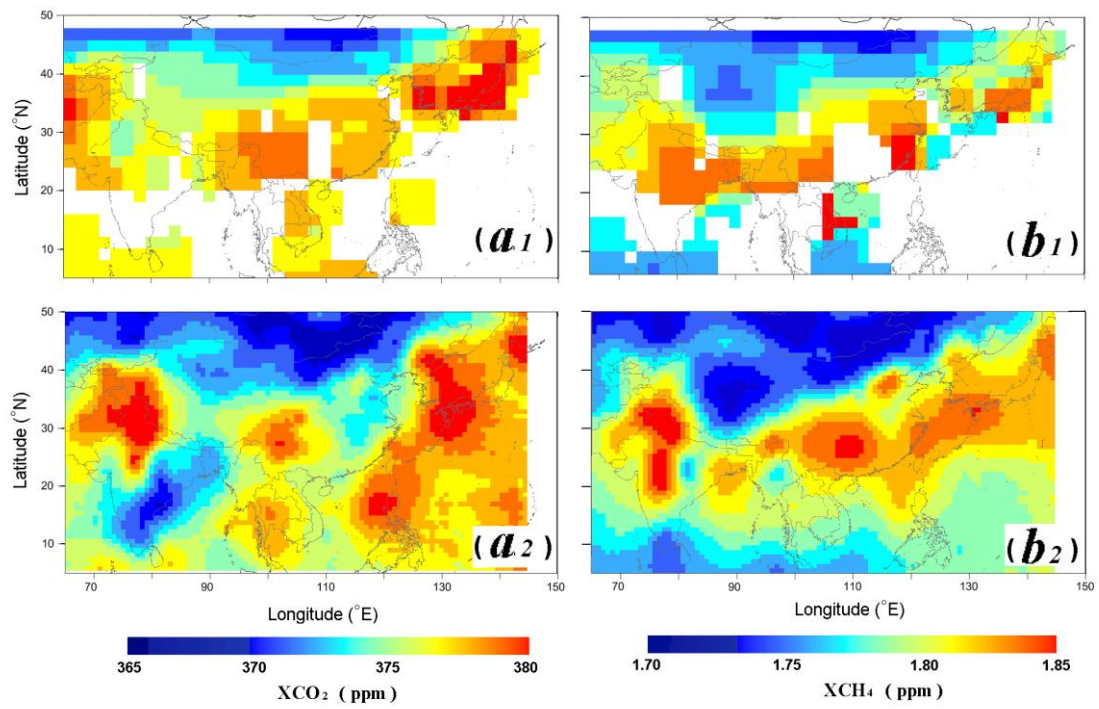
Figure 13. Comparison of FTS Level 3 data and FTS Level 2 Kriging interpolation data in September 2009: (*a*1) and (*a*2) are XCO_2 of FTS Level 3 data and FTS Level 2 Kriging interpolation data, respectively, (*b*1) and (*b*2) are XCH_4 of FTS Level 3 data and FTS Level 2 Kriging interpolation data, respectively